



# Experimental and analytical study on homogeneous and layered Al matrix syntactic foams under impact

Chen Liang, Yuyuan Zhao<sup>\*</sup>

School of Engineering, University of Liverpool, Liverpool L69 3GH, UK

## ARTICLE INFO

### Keywords:

Metal matrix syntactic foam  
Peak stress  
Impact ductility  
Impact wave propagation  
Stress-strain evolution

## ABSTRACT

Al matrix syntactic foams have been widely studied as impact protection materials. The impact behaviour of syntactic foams, especially for non-homogeneous structures, however, is not well understood. The impact response of Al matrix syntactic foams with both homogeneous and layered structures were studied experimentally and theoretically. Layered structures composed of large- and small-particle layers provided lower impact peak stress and higher ductility than the average values of the large- and small-particle layers. The energy absorption capacity of the layered structures is the sum of the energy absorption capacities of the constituent layers. An analytical model for stress and strain evolutions in Al matrix syntactic foams during impact was developed. The contact stress, inertia stress and base as a function of time was calculated as a function of impact velocity. The analytical model captures the key characteristics of stress fluctuation during impact. The predictions of the base stress agreed reasonably well with the experimental results, showing stress fluctuation with similar time interval and amplitude.

## 1. Introduction

Aluminium matrix syntactic foams (AMSFs) are a novel class of lightweight materials, which use hollow or porous ceramic particles such as alumina cenospheres [1,2], fly ash [3,4] or E-spheres [5] to reinforce the aluminium matrix. The main role of the particles or microballoons is to introduce porosity. AMSFs offer advantages of low weight, high specific stiffness, improved strength and high damage tolerance due to their mechanical energy absorption capabilities. These properties give AMSFs many applications such as cores in sandwich structures, crash protectors and damping panels [6].

The manufacture and mechanical properties of AMSFs with homogeneous structures have been widely studied. AMSFs were normally manufactured by the infiltration casting method and their compressive and energy absorption behaviours were investigated [7]. The effects of Al volume percentage, bimodal ceramic microspheres and Al particle toughening on the compressive and energy absorption properties of AMSFs have been studied [8,9]. Tao and Zhao [10] studied the compressive failure mechanisms of AMSFs through observations of the un-confined and confined compression response. The impact response of AMSFs have also been studied by both experiment and simulation [11, 12].

For porous metallic foams, energy absorption function is usually affected by porous structure. While hollow spheres can be divided into different densities and sizes by flotation methods and sieves. Then it is possible to designing specific syntactic foams to meet application demands with the variety of hollow spheres [13].

Functionally graded syntactic foams exhibit a gradual and controlled positional change of at least one property and often have desirable properties meeting the increasing demand in many industries [14–16]. The traditional way of manufacturing graded syntactic foams is fabricating each layer independently and subsequently bonding them together with an adhesive like epoxy. While fabricating the layers independently can easily tailor the physical and mechanical properties of each layer, layered syntactic foams manufactured from this approach have poor structural integrity between the layers. Graded syntactic foam components fabricated in one process by infiltration casting provide better structural integrity and superior mechanical properties [17].

Many efforts have been made to investigate the mechanical properties of syntactic foams under impact [18–20]. The majority of these studies, however, are largely confined to experimental characterisation or numerical modelling of stress - strain developments. Mechanistic understanding of the stress - strain evolutions and the role played by impact waves is still very limited. Karagiozova *et al.* [21] and Zheng *et al.*

<sup>\*</sup> Corresponding author: School of Engineering, University of Liverpool, Liverpool L69 3GH, UK.

E-mail address: [yyzhao@liverpool.ac.uk](mailto:yyzhao@liverpool.ac.uk) (Y. Zhao).

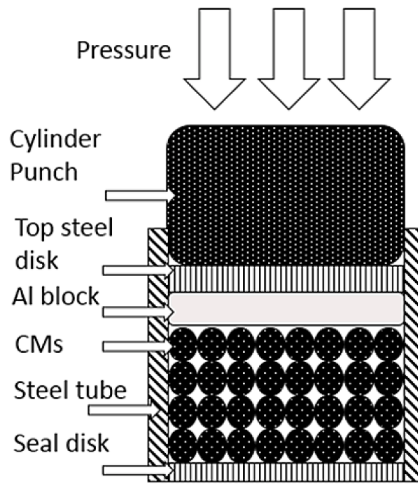


Fig. 1. Illustration of infiltration casting.

[22] proposed analytical models for stress evolutions in density-graded cellular materials based on the propagation of compaction waves and compared the analytical results with numerical simulation results. These models failed to capture one of the most important features of all experimental results - the fluctuation in stress evolution caused by propagation of impact waves. Rousseau *et al.* [23] made observations of stress fluctuation in syntactic foam samples by placing sensors at different locations. Rostilov and Ziborov [24] demonstrated the two-wave configuration stress evolution in syntactic foam under impact and used the Hugoniot states to describe the shocked states behind the wave front. Up to date, a mechanistic explanation of stress-strain evolutions in syntactic foams, especially with graded or layered structures, under impact is still lacking.

This study investigates the stress-strain evolution in AMSFs with homogeneous and layered structures under impact experimentally. An analytical model is developed to predict the stress and strain evolutions inside the AMSFs during impact. The theoretical predictions are compared with the experimental results.

## 2. Experimental

The AMSF samples were produced by infiltration casting [25], as shown schematically in Fig. 1, using a 6082 Al alloy and a hollow ceramic microsphere (CM) powder supplied by Envirospheres Pty Ltd. The CM powder has a composition of ~60% SiO<sub>2</sub>, ~40% Al<sub>2</sub>O<sub>3</sub> and 0.4-0.5% Fe<sub>2</sub>O<sub>3</sub> by weight and was separated into different particle size ranges. Two subset powders with particle size ranges of 75-150  $\mu$ m and 250-500  $\mu$ m, designated as small (S) and large (L), respectively, were used in the experiments. The two CM powders have a similar density of 0.66 g/cm<sup>3</sup>. Before infiltration, a steel tube, sealed by a circular steel disc at bottom, was filled either with one layer of the same CM powder or with two or three layers of different CM powders. An Al alloy block was then placed on top of the CM powder(s) and another circular steel disc was placed above the Al block. The assembly was heated to 755  $^{\circ}$ C for 30 min in an electric furnace before being moved to a hydraulic machine where the molten Al alloy was compressed into the voids between the CM particles. After solidification, the resultant AMSF sample was removed from the steel tube and ground into cuboid specimens with dimensions of 15  $\times$  15  $\times$  15 mm for quasi-static compression tests and 10  $\times$  10  $\times$  20 mm for impact tests.

The AMSF specimens are designated by the CM powders used in the specimens. L and S are homogeneous specimens containing large and small powders, respectively. LS is a two-layered specimen containing 50% large and 50% small powders. LSL is a three-layered specimen containing 25% large, 50% small and then 25% large powders. All the

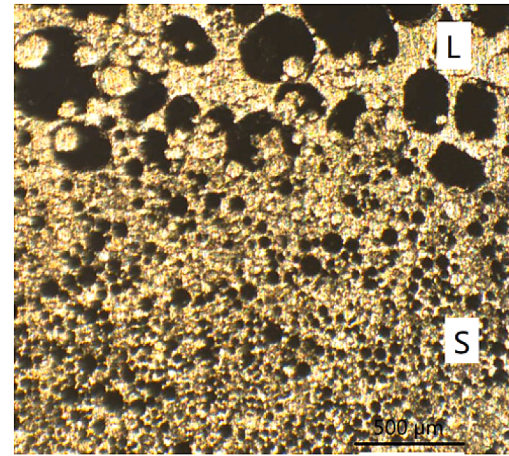


Fig. 2. Optical micrograph of a layered AMSF sample showing the interface between the two dissimilar layers.

Table 1  
Impact energies applied to the AMSF specimens.

Specimen	Impact velocity (m/s)	Impact energy (J)	Specific impact energy (J/g)
L	3.3	80	40
	3.7	100	50
	4	120	60
	4.3	140	70
S	1.7	20	10
	2.4	40	20
	2.9	60	30
	3.3	80	40
LS	3.3	80	40
	3.7	100	50
	4	120	60
	4.3	140	70
LSL	2.9	60	30
	3.3	80	40
	3.7	100	50
	4	120	60

AMSF specimens contain approximately 55% CM particles and have a density approximately 1.64 g/cm<sup>3</sup>. Fig. 2 shows the microstructure of a layered AMSF specimen, highlighting the interface between the two dissimilar layers.

Quasi-static compression tests were conducted on an Instron 4045 machine with a strain rate of 0.001 /s up to a strain of approximately 0.7. The specimens were lubricated with oil to reduce friction between the specimen and the platens.

Impact tests were conducted using an instrumented drop-weight tower. The specimen was supported by a solid steel base. A hammer with a mass of 15 kg, attached to a carriage guided by two vertical steel bars, was raised to a height varying between 0.2 – 1.2 m to give a varying impact energy of 20 – 140 J, equivalent to a specific impact energy or impact energy per unit specimen mass of 10 – 70 J/g. Table 1 shows the impact energy subjected by each specimen. A Kistler 9061A piezo-electric load-cell, with a maximum capacity of 200 kN, was used to measure the force-time history. The impact force signal was recorded using the Data Flow Plus software. The hammer velocity and displacement were measured using a MotionPro-X4 high speed camera at a frame rate of 5000 fps and analysed using the ProAnalyst software. Three samples were tested under each impact energy for each type of AMSFs.

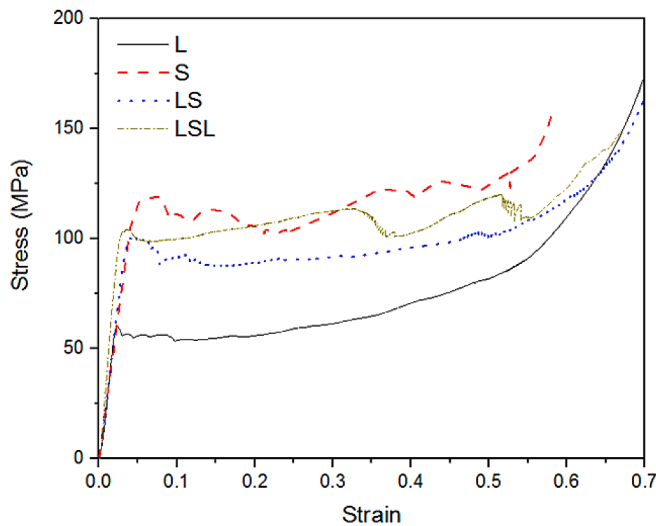


Fig. 3. Compressive stress-strain curves of AMSF samples.

Table 2

Yield strength, Young's modulus and energy absorption of the four AMSF specimens.

Specimen	Yield stress (MPa)	Young's modulus (GPa)	Plastic modulus (GPa)	Energy absorption (J/g)
L	60	3.0	0.024	20.3
S	120	2.9	0.019	32.6
LS	100	3.0	0.018	27.4
LSL	104	3.3	0.021	30.8

### 3. Experimental results

#### 3.1. Compressive behaviour

Fig. 3 exhibits typical quasi-static compressive stress-strain curves of AMSFs. Specimen L has a much lower strength than specimen S but a better ductility, characterised by a much smoother plateau region. The strengths of the layered specimens LS and LSL fall between those of specimens L and S, with LSL having a slightly higher yield stress than LS. The difference in strength between L and S is due to their different structural characteristics. Ceramic microspheres in L are large and generally porous, while those in S are small and mainly hollow. For the same density or porosity, hollow particles are stronger than porous ones and particle strength generally decreases with particle size [10]. The difference in strength between LS and LSL, which have the same amounts of L and S, is due to the layer thickness effect. In layered structures, the weaker L layers deform before the stronger S layers. However, the weaker layer is confined by the neighbouring stronger layers and exhibits a barrelling phenomenon. A thinner layer is generally stronger than a thicker layer due to decreased barrelling [17], resulting in LSL being stronger than LS.

Table 2 shows the yield strength, Young's modulus, plastic modulus and specific energy absorption (up to 0.5 strain) of the four AMSF specimens. Plastic modulus is defined as the gradient of the stress-strain curve in the plastic region. Because the actual stress-strain curves in this region are not linear, the plastic modulus values were obtained by linear fitting of the stress-strain curves in the plastic region. All specimens have a similar Young's modulus, as they have the same amount of CM particles of 55% and same amount of porosity. The yield stress and energy absorption in the layered LS and LSL specimens are approximately the averages of the L and S specimens, although LSL has a higher stress than LS.

It is interesting that the layered specimens have one yield point,

Table 3

Impact behaviour of AMSF specimens at a range of impact energies. D denotes ductile, B brittle, and DB ductile-brittle

Specimen	20 J	40 J	60 J	80 J	100 J	120 J	140 J
L				D	D	D	D
S	D	DB	B	B			
LS				D	D	D	DB
LSL			D	D	DB	B	

which is different from a previous study on stacked layered syntactic foams [16], which showed a layer-by-layer deformation. As the layered specimens in this work were manufactured by infiltration casting in one step, there is a gradual change in microstructure at the interface between adjacent layers (Fig. 2). It seems that the strong bonding between the integral layers in the specimens has led to deformation of the layers in a coordinated rather than independent manner.

#### 3.2. Impact behaviour

Impact tests were conducted at various impact energies from 20 J to 140 J, with an increment of 20 J, to identify the transition from ductile to brittle behaviours. Table 3 shows the range of impact energy covering the ductile-brittle transitions for the AMSF specimens. With increasing impact energy, the behaviour changed from ductile deformation, to semi-brittle deformation with cracks emerging, and finally to brittle fracture. For specimen S, cracks emerged at an impact energy of 40 J (20 J/g) at a strain of 0.09. Although it had a lower energy absorption of 4.5 J/g at the strain of 0.09 under quasi-static loading, it deformed plastically under quasi-static loading and had an energy absorption capacity of 32.6 J/g at a strain of 0.5. It means that specimen S cannot fulfil its energy absorption capacity under impact loading due to its brittleness. In contrast, specimen L remained ductile at a high impact energy of 140 J (70 J/g), although it has a low energy absorption of 20.3 J/g under quasi-static loading. The more brittleness in homogeneous specimen S than L is due to the much larger number of microspheres in S than in L. Because the contact points between the brittle ceramic microspheres are potential crack initiation sites, more microspheres result in more contact points, which in turn increase the possibility of crack initiation and thus more brittleness. Furthermore, more microspheres lead to thinner Al matrix between the microspheres, which can also compromise the ductility, because ductility is provided by the metal matrix in AMSFs [26].

Table 3 also shows that the layered specimens are significantly more ductile than the brittle layer and have better ductility than the average of their constituent layers under impact. Specimen LS remained ductile at 120 J, while specimen LSL became brittle at 100 J. As the only difference between specimens LSL and LS is distribution of layer L, it suggests that two thinner L layers lead to lower ductility than one thicker L layer. In a layered AMSF, a thicker soft layer constrained by a neighbouring hard layer or impactor barrels more than a thinner soft layer. The single soft layer in LS is expected to absorb more impact energy than the two soft layers in LSL. This effectively reduces the stress exerted on the brittle hard layer and improves the ductility of the layered sample.

Fig. 4 shows stress evolution in the AMSF specimens under an impact energy of 80 J. The test results of three specimens each for L and S are presented to illustrate the good reproducibility. Similar to the yield stress under quasi-static loading, specimen L has a lower peak stress than specimen S under impact, while the layered specimens have an intermediate peak stress between those of specimens L and S. Fig. 5 shows the effect of impact energy on peak stress for the four specimens. Peak stress increases linearly with impact energy for both homogeneous and layered structures. The peak stresses of the layered specimens are closer to that of the soft layer L than to that of the hard layer S. The reduction in peak stress in the layered structures is because the soft layer L absorbs most

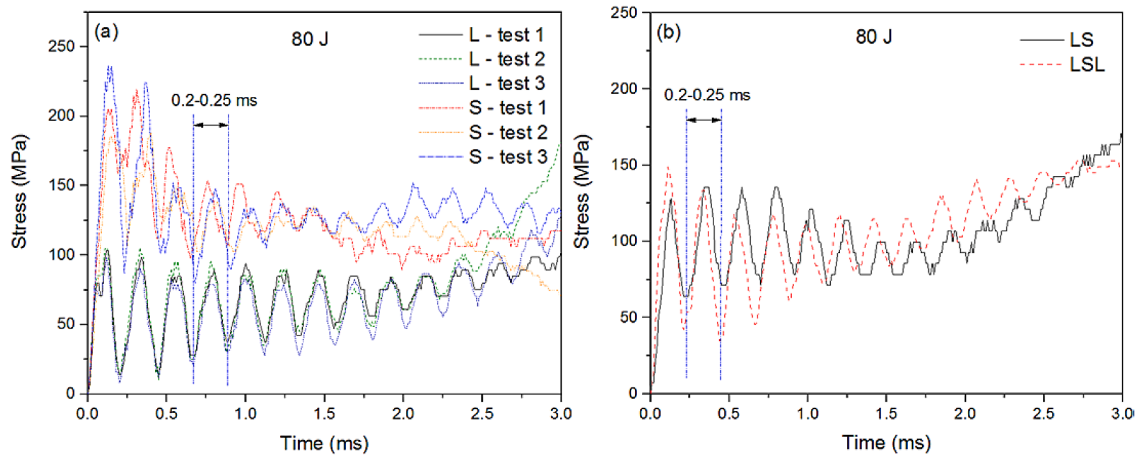


Fig. 4. Stress evolution under an impact energy of 80 J for (a) homogenous and (b) layered AMSF specimens.

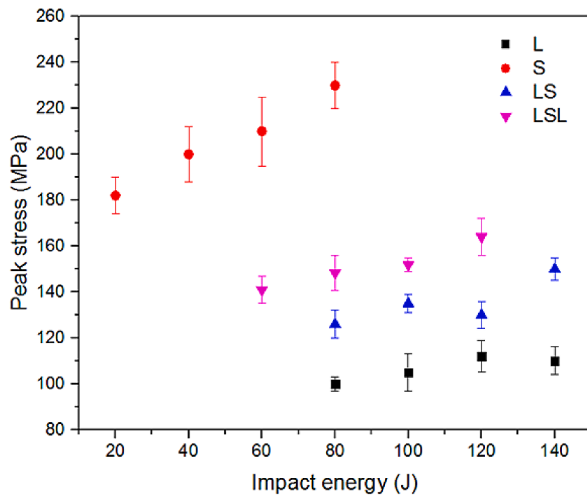


Fig. 5. Effect of impact energy on peak stress in AMSF specimens.

energy in the early stage. This explains the ductility increase in the layered structures. Specimen LSL has a higher peak stress than LS, which leads to a higher chance of fracture under impact loading, as confirmed by the ductility transition results in Table 3.

Fig. 4 shows that the stress in all the AMSF specimens under impact fluctuated with a nearly constant time interval of 0.2-0.25 ms. Stress

evolution under impact is the result of plastic wave propagation generated by the impact. Stress fluctuation is caused by plastic wave rebound inside the specimen. As all the AMSF specimens have a similar Young's modulus and plastic modulus, they have a similar wave propagation speed and therefore a similar fluctuation time interval.

Fig. 6 shows the relative contributions from the constituent layers to the total strain in the layered specimens. The contributions were obtained experimentally from the images acquired by the high speed camera. Specifically, for each frame at each time interval, the thicknesses of the constituent layers were measured and the strains were calculated, from which the relative contributions were obtained. Fig. 6 shows that most deformation in LS occurred in the soft layer L in the beginning (0 - 0.6 ms). Thereafter, deformation in the hard layer S increased until the soft layer L was densified. The contributions from the two layers then became equal, i.e., 50%-50%. LSL showed a similar trend; most deformation in the beginning occurred in L; contribution from deformation in S increased gradually until the contributions were spread equally in all layers at the end, i.e., 25%-50%-25% in L-S-L. Similar to a previous report [18], the top and bottom sides of a layered sample have similar chance to initiate deformation under impact. Generally, once deformation is initiated in one side, deformation occurs preferentially in this side. The other side follows when its condition for deformation becomes favourable.

Effect of strain rate on compressive deformation behaviour and failure mechanism of syntactic foams is well documented [27-29]. Syntactic foams exhibit higher strengths, and therefore higher energy absorption capacities, under impact loading than in quasi-static compression. Increasing strain rate up to a critical value, which is

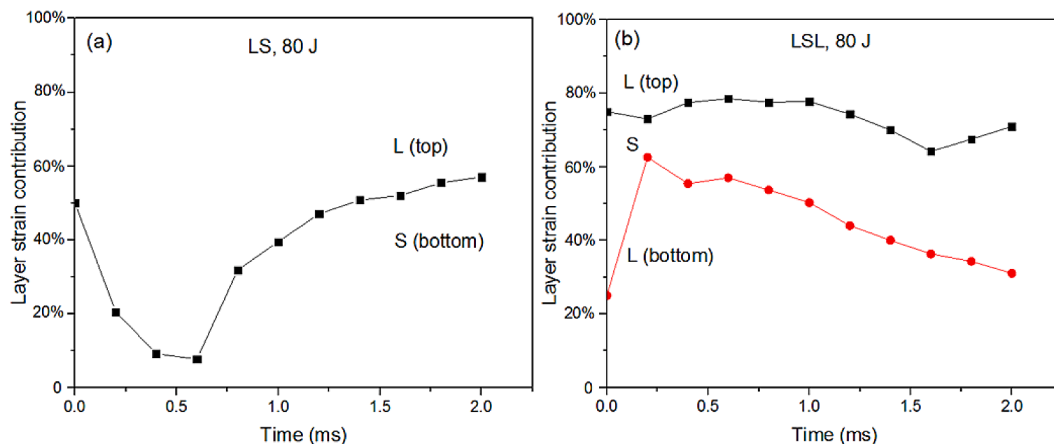


Fig. 6. Contributions to total strain from individual layers in layered specimens (a) LS and (b) LSL.



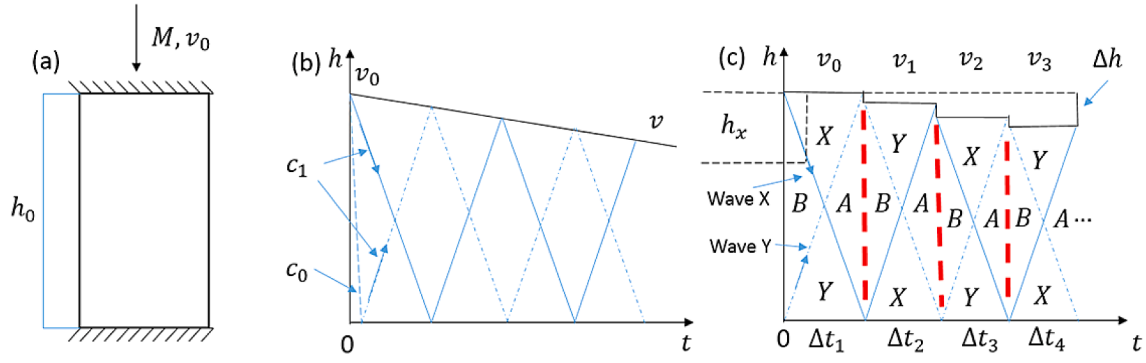


Fig. 7. Impact waves inside an AMSF specimen under impact, (a) schematic of impact, (b) impact wave and impact velocity evolution, and (c) simplified impact wave evolution model.

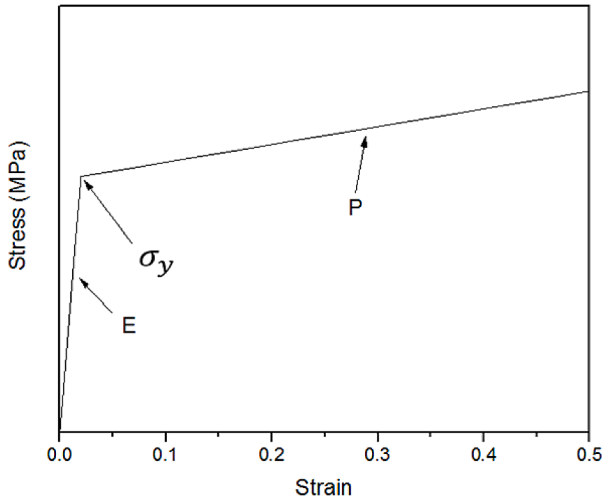


Fig. 8. Idealised mechanical behaviour of AMSFs, indicating yield stress  $\sigma_y$ , elastic modulus  $E$  and plastic modulus  $P$ .

material dependent, increases the impact strength. The underlying mechanism for the increased stress and energy absorption under impact loading is the acceleration and deceleration of particles inside the material due to plastic waves, as shown in the theoretical analysis to be described in the following section. The plastic waves result in uneven distribution of stress in the material. High local stress increases the chance of crack initiation and propagation and can change the failure mechanism from ductile deformation to brittle fracture.

The different behaviours of homogeneous specimens L and S under impact loading are in agreement with a previous study [28], which found AMSF with finer cenospheres exhibited higher strain rate sensitivity. The effect of cenosphere size on the deformation behaviour was attributed to different degrees of contribution of the aluminium matrix [28]. While the deformation of the AMSF with finer cenospheres is primarily controlled by the deformation of the cenospheres, the aluminium matrix in the AMSF with coarser cenospheres also contributes to the deformation. Because the aluminium matrix is less sensitive to strain rate [30], AMSFs with coarser microspheres are more ductile and less sensitive to strain rate.

The alleviation of brittleness of the S layer in layered AMSFs is due to the confinement effect. The confinement effect on the failure mechanism has been demonstrated in an epoxy syntactic foam [31]. The confined samples showed an elastic-plastic behaviour while the unconfined specimens showed an elastic-brittle behaviour. The same effect exists in the layered AMSFs, where the L layers restrict the lateral movement of the S layer, improving the ductility of the S layer.

## 4. Theoretical analysis

### 4.1. Analytical model

Let us consider an AMSF specimen with an initial height  $h_0$ , situated on a frictionless flat rigid die and subjected to compression by an upper die of mass  $M$ , moving with an initial speed  $v_0$ , as shown in Fig. 7 (a). Based on the compressive stress-strain curves of the AMSF specimens (Fig. 3), the AMSF can be assumed to be an ideal elastic-linear strain-hardening material with yield stress  $Y$ , elastic modulus  $E$  and plastic modulus  $P$ , as shown schematically in Fig. 8. According to the impact theory [32], impact loading creates an elastic wave  $c_0$  and a plastic wave  $c_1$  in the specimen; these two waves propagate inside the specimen as shown in Fig. 7(b). The speeds of elastic and plastic waves are:

$$c_0 = \sqrt{\frac{E}{\rho}}; c_1 = \sqrt{\frac{P}{\rho}} \quad (1)$$

where  $\rho$  is the density of the specimen, which changes in the case of a porous material as plastic deformation proceeds.

All the AMSF specimens in this work have a similar elastic modulus  $E$  ( $\approx 3$  GPa) and plastic modulus  $P$  ( $\approx 0.02$  GPa), with only yield stress  $\sigma_y$  being different (60–120 MPa), as can be seen in Fig. 3. For simplicity, we can assume elastic modulus and plastic modulus are constant and independent of the specimens. The elastic modulus  $E$  is significantly higher than the plastic modulus  $P$ . As a consequence, the elastic wave speed,  $c_0$ , is nearly one order of magnitude higher than the plastic wave speed,  $c_1$ . We can neglect the time the elastic wave travels from the top to the bottom of the specimen and assume that the two plastic waves, X and Y, emerge simultaneously from the top and bottom, respectively, of the specimen at the outset of impact as shown in Fig. 7.

Stress-strain evolution in the specimen is a result of the propagation of the two plastic waves, designated as wave X and wave Y, as shown in Fig. 7c. In each cycle when the two waves travel from one end to the other, four different stress zones can be identified in the specimen: before the waves pass (zone B), passed by wave X (zone X), passed by wave Y (zone Y) and after both waves passed (zone A). The stresses in these four zones can be determined from the yield stress of the material, the elastic wave speed, the plastic wave speed and the impact velocity, using a set of equations well defined by the impact theory [32]. When the waves reach the end of the specimen, they bounce back and travel to the other end. The same four zones can be identified in this new cycle, each accompanied by a stress increase. This process is repeated for a number of cycles until the impact energy is consumed and the impact velocity, or hammer velocity, is reduced to zero.

An explicit analytical solution of the stress evolution during impact is only possible if the impact velocity remains constant. In practical impact tests, however, the impact velocity decreases with time as the kinetic energy of the hammer is gradually absorbed by the AMSF specimen.

Fortunately, the plastic wave speed ( $c_1 \approx 108$  m/s) is significantly higher than the impact velocity ( $v_0 \approx 1.7$ – $4.3$  m/s). We can neglect the change in impact velocity and the change in strain within one cycle when the plastic waves travel from one end to the other and assume a step change in the impact velocity and a step change in the strain from one cycle to the next. The wave propagation process can be split into discrete steps, marked as time periods  $\Delta t_1$ ,  $\Delta t_2$ ,  $\Delta t_3$ , etc., as shown in Fig. 7c. Each step represents one cycle and corresponds to plastic waves traveling the specimen length from one end to the other. While the impact velocity, specimen length, density, stress and strain change from one cycle to the other, they are considered constant within each cycle and can be calculated analytically.

#### 4.1.1. Stress-strain evolution inside the specimen

Up to three stress zones are produced in the specimen at any one time with the propagation of the waves, namely zone X, zone Y and the middle zone, as shown in Fig. 7c. The middle zone is designated as zone B before the two plastic waves pass and as zone A after both waves have passed. In zone B, a stress equal to the yield stress of the specimen is produced instantly when the elastic wave travels from top to bottom. In zone X, an additional stress is generated by the plastic wave X. Similarly, an additional stress is generated by the wave Y in zone Y, but with a different magnitude from zone X due to different wave direction to the impact. In zone A, a cumulative additional stress is generated by the two plastic waves. When each wave bounces back at the top or bottom edge of the specimen, it creates a stress increment. As a result, the stress in each zone is increased successively in the following cycles of wave propagation.

Based on the impact theory for the constant impact velocity case [27], the stresses in the different zones in the first cycle of wave propagation can be expressed as follows:

$$\begin{cases} \sigma_{X(1)} = \sigma_y \left( 1 - \frac{c_1}{c_0} \right) + \rho_0 c_1 v_0 = \sigma_y \left( 1 - \sqrt{\frac{P}{E}} \right) + \sqrt{\rho_0 P} v_0 \\ \sigma_{Y(1)} = \sigma_y \left( 1 + \sqrt{\frac{P}{E}} \right) \\ \sigma_{B(1)} = \sigma_y \\ \sigma_{A(1)} = \sigma_y + \sqrt{\rho_0 P} v_0 \end{cases} \quad (2)$$

where  $\sigma_X$ ,  $\sigma_Y$ ,  $\sigma_B$  and  $\sigma_A$  are the stresses in zones X, Y, B and A, respectively,  $\rho_0$  is the initial density of the specimen before any plastic deformation, and the subscript 1 in brackets indicates the first cycle in the time period  $\Delta t_1$ .

Taken into account the change in impact velocity between adjacent cycles, the stress in each zone in the current cycle of wave propagation is increased by a fixed amount from the previous cycle and can be obtained as follows:

$$\sigma_{z(n)} = \sigma_{z(n-1)} + \sqrt{\rho_{n-1} P} v_{n-1} \quad (3)$$

where  $z$  designates the zone, i.e., X, Y, A or B, the subscript  $n$  in brackets indicates the  $n^{\text{th}}$  cycle of wave propagation,  $(n-1)$  indicates the previous cycle,  $\rho_{n-1}$  is the density of the specimen in the previous cycle and  $v_{n-1}$  is the impact velocity in the previous cycle.  $n$  can also be understood as the number of times each plastic wave has travelled through the full length of the specimen forwards and backwards.

According to the idealised mechanical behaviour of the AMSFs shown in Fig. 8, the strain in each zone can be easily obtained from the stress by:

$$\varepsilon_z = \frac{\sigma_z - \sigma_y}{P} \quad (4)$$

where  $\varepsilon_z$  and  $\sigma_z$  are the strain and stress in zone  $z$ , with  $z$  being X, Y, B or A. The strain in each zone is manifested in a displacement, which depends on the size of the zone. The total strain of the specimen at any time

can be calculated from the cumulative displacements from all the zones present at this particular time by:

$$\begin{cases} = \frac{h_X \varepsilon_X + h_Y \varepsilon_Y + h_B \varepsilon_B}{h} \quad \left( 0 \leq t \leq \frac{\Delta t}{2} \right) \\ = \frac{h_X \varepsilon_X + h_Y \varepsilon_Y + h_A \varepsilon_A}{h} \quad \left( \frac{\Delta t}{2} < t < \Delta t \right) \end{cases} \quad (5)$$

where  $h_X$ ,  $h_Y$ ,  $h_B$  and  $h_A$ , are the unstrained heights of each zone,  $\varepsilon_X$ ,  $\varepsilon_Y$ ,  $\varepsilon_B$  and  $\varepsilon_A$  are the strains of zones X, Y, B and A, respectively,  $h$  is the height of the specimen in the current cycle,  $t$  is the time of wave propagation from the onset of the current cycle, and  $\Delta t$  is the duration of the current cycle. The heights of the respective zones change with time in each cycle as follows:

$$\begin{cases} h_X = h_Y = c_1 t; \quad h_B = h - 2c_1 t \quad \left( 0 \leq t \leq \frac{\Delta t}{2} \right) \\ h_X = h_Y = h - c_1 t; \quad h_A = 2c_1 t - h \quad \left( \frac{\Delta t}{2} < t < \Delta t \right) \end{cases} \quad (6)$$

The height of the specimen,  $h$ , the density of the specimen,  $\rho$ , the duration of the wave propagation cycle,  $\Delta t$ , and the impact velocity,  $v$ , change from cycle to cycle. The change in the height of the specimen between two successive cycles is the distance travelled by the hammer, so the height of the specimen in the current cycle can be calculated from the height in the previous cycle by:

$$h_n = h_{n-1} - v_{n-1} \Delta t_{n-1} \quad (7)$$

The duration, or time period, of the wave propagation cycle is simply:

$$\Delta t_{n-1} = \frac{h_{n-1}}{c_{1(n-1)}} = h_{n-1} \sqrt{\frac{\rho_{n-1}}{P}} \quad (8)$$

The decrease in impact velocity is due to the kinetic energy of the hammer being consumed by the plastic deformation of the AMSF specimen. In each cycle, the energy conversion can be expressed by:

$$\frac{1}{2} M v_{n-1}^2 - \frac{1}{2} M v_n^2 = A \left( \frac{\sigma_{B(n-1)} + \sigma_{A(n-1)}}{2} \right) v_{n-1} \Delta t_{n-1} \quad (9)$$

where  $A$  is the cross sectional area of the specimen. The left hand side of Eq. (9) is the kinetic energy loss of the hammer in a cycle. The right hand side is the energy absorbed by the plastic deformation in the cycle, which is equal to the product of the force and displacement in the specimen. It should be noted that the stress in the specimen in a cycle is not constant but changes from  $\sigma_B$  at the beginning to  $\sigma_A$  at the end of the cycle, so the average stress is used in determining the energy absorbed.

Re-arranging Eq. (9) gives the impact velocity of the current cycle as:

$$v_n = \sqrt{v_{n-1}^2 - \frac{A(\sigma_{B(n-1)} + \sigma_{A(n-1)})v_{n-1}}{M}} \quad (10)$$

As the plastic deformation of a porous material is associated with the collapse of pores, the cross sectional area of the specimen does not change when the height of the specimen changes during plastic deformation. The density of the specimen is therefore inversely proportional to specimen height and can be calculated by:

$$\rho_n = \rho_{n-1} \frac{h_{n-1}}{h_n} \quad (11)$$

#### 4.1.2. Base stress

When a specimen is subjected to the impact of a hammer on the top, as shown in Fig. 7(a), a contact stress is generated on the top of the specimen by the hammer and an inertia stress is induced inside the specimen due to the elastic and plastic waves. There is a difference between the contact stress at impact and the stress transmitted through the specimen to the base [33]. The transmitted stress exerted on the supporting base, or base stress, is the sum of the contact stress,  $\sigma_c$ , and the

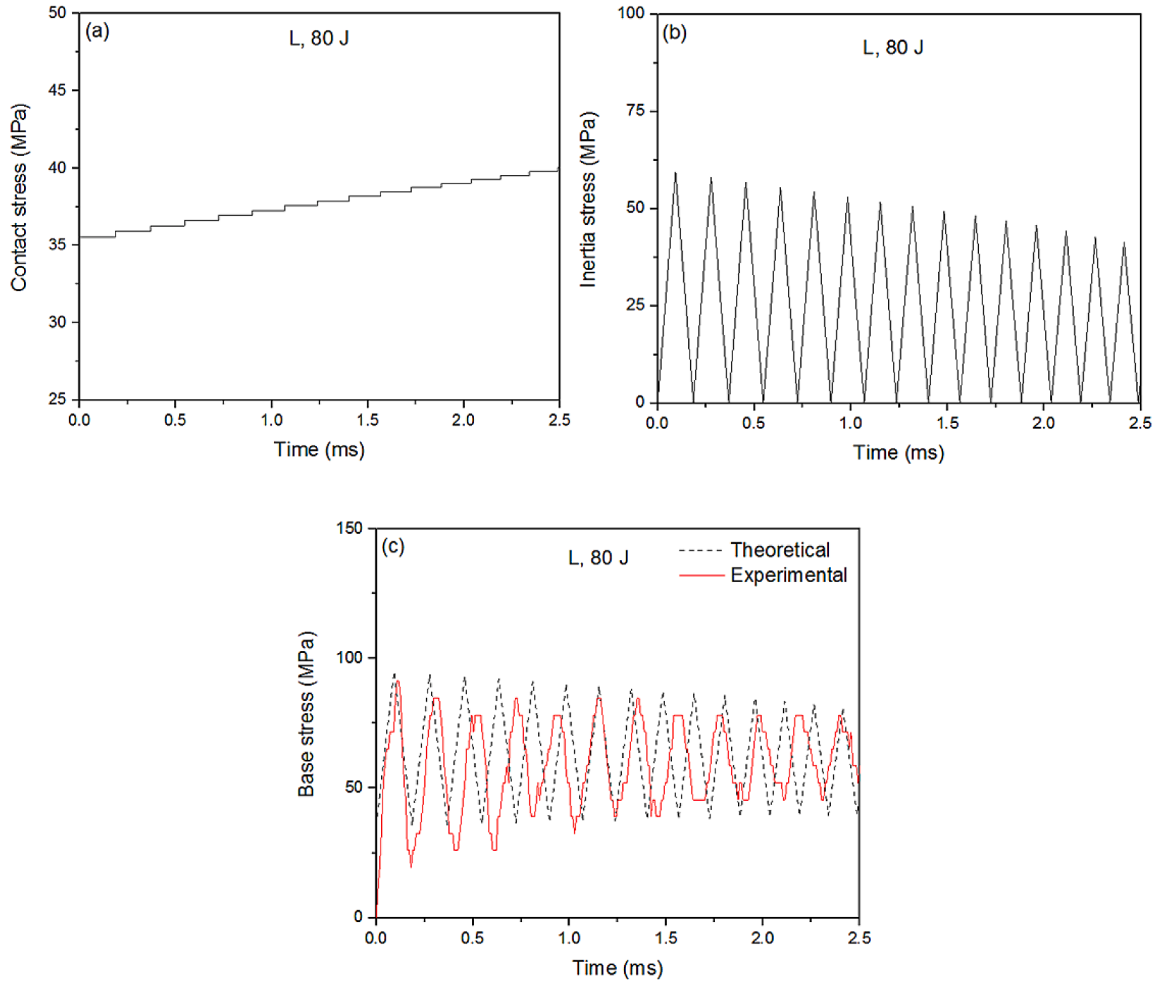


**Fig. 9.** Theoretical stress evolutions in the homogeneous AMSF specimen L subjected to an impact energy of 80 J: (a) contact stress, (b) inertia stress, and (c) base stress compared to experimental result.

total inertia stress,  $\sigma_i$ :

$$\sigma_b = \sigma_c + \sigma_i \quad (12)$$

The contact stress occurring at the hammer-specimen interface is proportional to the deceleration and can be estimated from the velocity change of the impact hammer by:

$$\sigma_c = \frac{M}{A} \frac{\Delta v}{\Delta t} \quad (13)$$

where  $\Delta v$  is the velocity change between two adjacent cycles, which can be calculated from Eq. (10), and  $\Delta t$  is the cycle time, which can be calculated from Eq. (8).

The inertia stress is caused by the moving particles in the specimen. The moving particles are confined to the zones behind the plastic waves, i.e., zones X and Y only. Neither of the two plastic waves has reached zone B and the two opposing waves have both passed zone A, so the particles in zones B and A are stationary. Therefore, the inertia stress is the sum of the height-weighted stresses in zones X and Y, relative to the initial specimen height. Given that the heights of zones X and Y are symmetric, the total inertia stress is:

$$\sigma_i = \frac{h_X(\sigma_X + \sigma_Y)}{h_0} \quad (14)$$

#### 4.2. Predictions and comparisons with experimental results for homogeneous structures

The theoretical results for the evolutions of the contact stress, inertia stress and base stress in the homogeneous AMSF specimens L and S, subjected to an impact energy of 80 J, are shown in Figs. 9 and 10, respectively. In the experiments, the impact stress was measured at the bottom of the specimen. It is equivalent to the base stress in Eq. (12), which is composed of the contact stress and the inertia stress. The contact stress is caused by the deceleration of the hammer or change of impact velocity (Eq. 13), which increases with time. As a consequence, the contact stress increases with time (Figs. 9a and 10a). The contact stress is sensitive to the yield stress of the material, hence the significant difference between specimens L and S. The inertia stress fluctuates because it is proportional to the height of zones X and Y (Eq. 14). In each impact cycle, it increases from zero at the outset to the maximum at the midpoint and then decreases to zero at the end of the cycle (Fig. 9b and Fig. 10b). This fluctuating inertia stress results in the fluctuation in the base stress and hence the experimentally measured stress. Specimen S has higher inertia stress than specimen L because the former has a higher yield stress.

The theoretical predictions agree reasonably well with the experimental results (Fig. 9c and Fig. 10c), especially for specimen L. The analytical model captures the key characteristics of stress fluctuation with fairly accurate predictions of time period and reasonable estimation of stress range of fluctuation. The considerable deviation in the fluctuation stress range for specimen S is due to its higher degree of

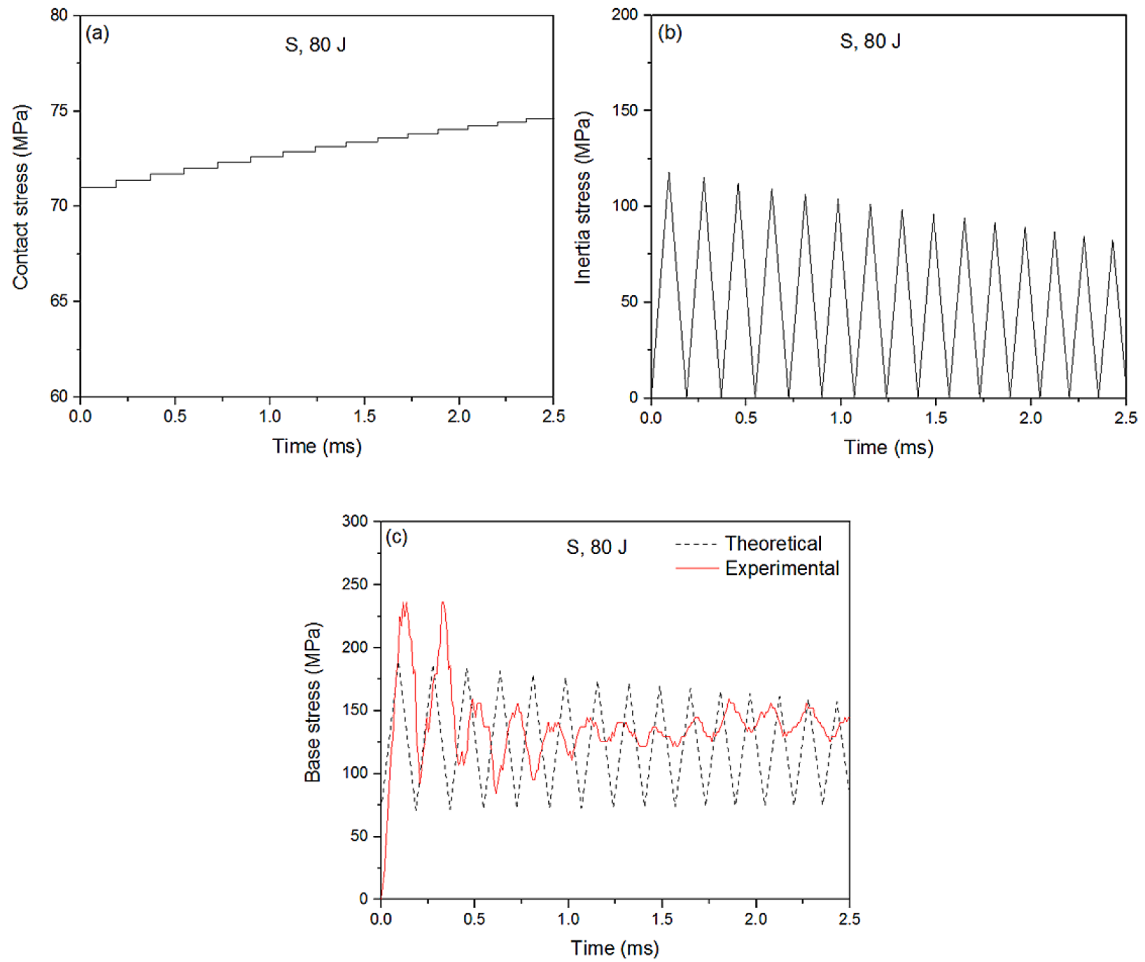


**Fig. 10.** Theoretical stress evolutions in the homogeneous AMSF specimen S subjected to an impact energy of 80 J: (a) contact stress, (b) inertia stress, and (c) base stress compared to experimental result.

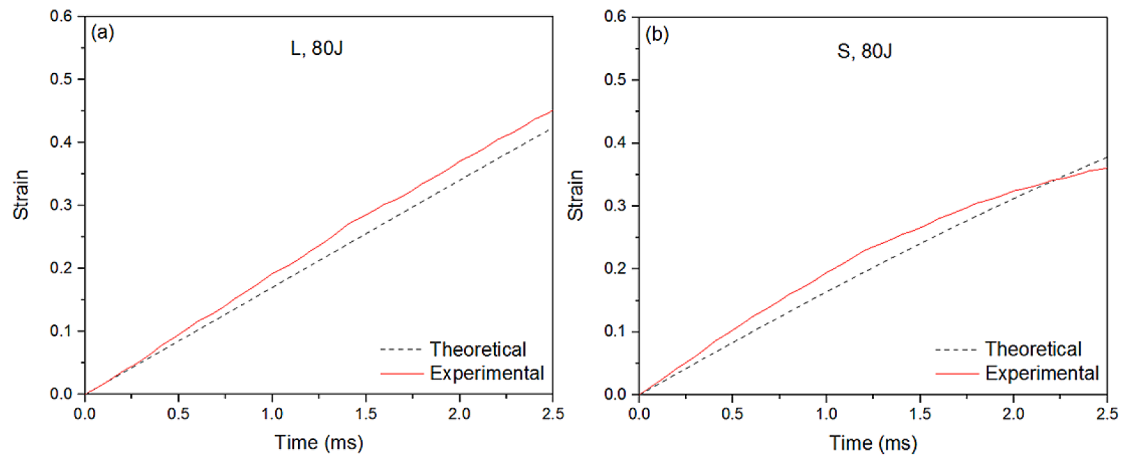


**Fig. 11.** Theoretical and experimental strain evolutions in the homogeneous AMSF specimens: (a) L, and (b) S.

brittleness. The analytical model assumes that the specimens undergo plastic deformation under impact without any fracture. In practice, micro or macro cracks emerge during impact, especially for more brittle specimens, which can release the stress and decrease the fluctuation range.

Fig. 11 compares the theoretical and experimental results of strain evolutions. The theoretical predictions by Eq. (5) agree well with the experimental values for both specimens L and S. Specimen S has lower

strain than specimen L under the same impact because it has a higher yield stress and therefore consumes more energy.

#### 4.3. Predictions and comparisons with experimental results for layered structures

The AMSFs L and S have a very similar density and plastic modulus, so the plastic waves in both L and S have nearly the same propagation



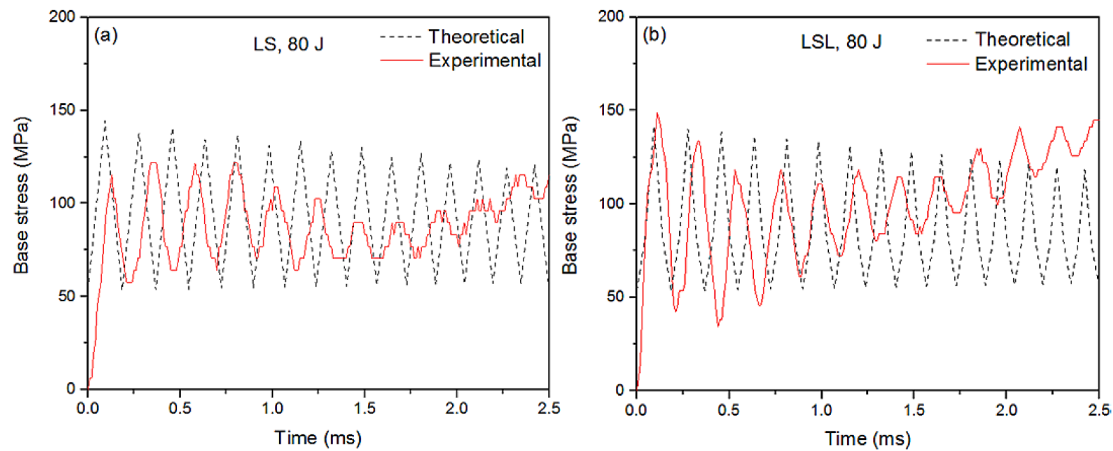


Fig. 12. Theoretical and experimental base stress evolutions in layered AMSFs: (a) LS, and (b) LSL.

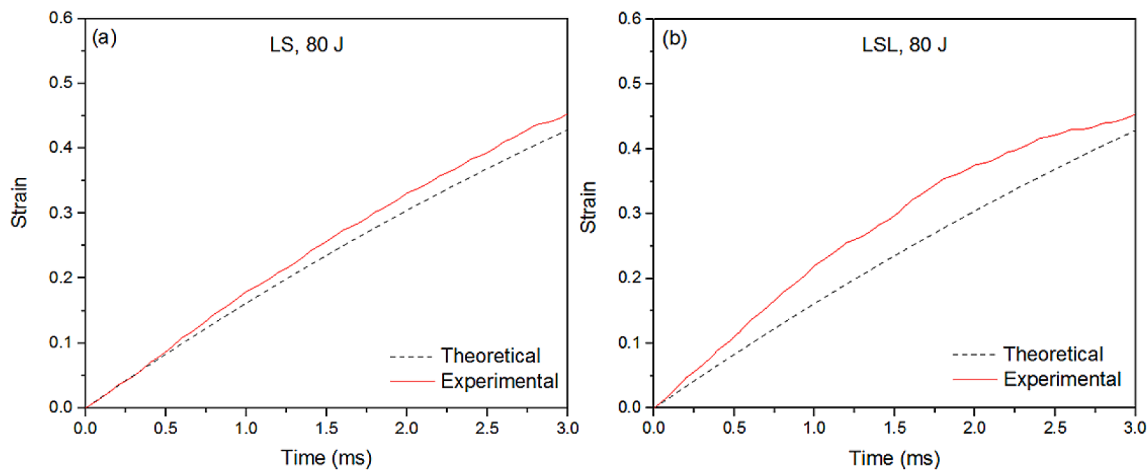


Fig. 13. Theoretical and experimental strain evolutions in layered AMSFs: (a) LS, and (b) LSL.

velocity. Consequently, the impact wave propagation in layered AMSF structures consisting of L and S layers is the same as that in homogeneous AMSF structures. The plastic waves in a layered AMSF specimen also propagate through the whole length of the specimen and reverberate in a cyclic manner, as shown in Fig. 7c. However, AMSFs L and S have different yield stresses. The L and S layers in a layered AMSF specimen experience different stresses and therefore have different strains. However, the amounts of plastic deformation in the layers in each cycle are small relative to the specimen height. The ratios of the layer thicknesses can be considered to remain the same during the impact. The analytical model developed for homogeneous structures can be applied directly to layered structures. The contact stress, inertia stress and base stress can be calculated in the same way, except local yield stress replacing global yield stress.

Figs. 12 and 13 compare the theoretical and experimental results of base stress and strain evolutions, respectively, in the layered LS and LSL AMSFs. Similar as in the case of homogeneous AMSFs, the analytical model captures the key characteristics of stress fluctuation with fairly accurate prediction of time period of stress fluctuation, reasonable estimation of stress range of fluctuation, and good prediction of strain development.

## 5. Conclusions

The impact response of AMSFs with both homogeneous and layered structures were studied experimentally. Layered structures LS and LSL

provided lower impact peak stress and higher ductility than the average values of L and S. The three-layer structure had higher peak stress and lower ductility than the two-layer structure. The energy absorption capacity of the layered structures is the sum of the energy absorption capacities of the constituent layers.

An analytical model for stress and strain evolutions in both homogeneous and layered AMSFs during impact was developed. The contact stress between the impact hammer and the specimen and the inertia stress generated inside the specimen as a function of time can be calculated as a function of impact velocity. The inertia stress is generated by the moving particles inside the specimen, due to the propagation of the two plastic waves caused by the impact loading. The base stress is the sum of the contact stress and the inertia stress. The model predictions of the base stress as a function of time agreed with the experimental results, showing stress fluctuation with similar time interval and amplitude.

## Declaration of Competing Interest

The authors declare that they have no known competing financial interests or personal relationships that could have appeared to influence the work reported in this paper.

## Acknowledgement

Liang would like to thank the China Scholarship Council and the

University of Liverpool for a PhD studentship.

#### Author statement

Chen conducted the experimental and analytical modelling work and drafted the manuscript. Zhao oversaw the whole project work, provided inputs to the theoretical analysis and assisted in writing the manuscript.

#### References

- [1] He MY, Zok FW, Kiser M. The mechanical response of ceramic microballoon reinforced aluminum matrix composites under compressive loading. *Acta Mater* 1999;47:2685–94.
- [2] Alizadeh M, Mirzaei-Aliabadi M. Compressive properties and energy absorption behavior of AlAl<sub>2</sub>O<sub>3</sub> composite foam synthesized by space-holder technique. *Mater Des* 2012;35:419–24.
- [3] Rohatgi PK, Gajdardziska-Josifovska M, Robertson DP, Kim JK, Guo RQ. Age-hardening characteristics of aluminum alloy-hollow fly ash composites. *Metall Mater Trans A* 2002;33A:1541–7.
- [4] Rohatgi PK, Daoud A, Schultz BF, Puri T. Microstructure and mechanical behaviour of die casting AZ91D-fly ash cenosphere composites. *Compos Part A*. 2009;40:883–96.
- [5] Zhao YY, Tao XF. Behaviour of metal matrix syntactic foams in compression. *Mater Sci Technol* 2009;(25):1785–94.
- [6] Goel MD, Matsagar VA, Gupta AK. Blast resistance of stiffened sandwich panels with aluminum cenosphere syntactic foam. *Int J Impact Eng* 2015;77:134–46.
- [7] Zhang LP, Zhao YY. Mechanical response of Al matrix syntactic foams produced by pressure infiltration casting. *J Compos Mater* 2007;41(17):2105–17.
- [8] Tao XF, Zhang LP, Zhao YY. Al matrix syntactic foam fabricated with bimodal ceramic microspheres. *Mater Des* 2009;30(7):2732–6.
- [9] Tao XF, Zhao YY. Compressive behavior of Al matrix syntactic foams toughened with Al particles. *Scripta Mater* 2009;61(5):461–4.
- [10] Tao XF, Zhao YY. Compressive failure of Al alloy matrix syntactic foams manufactured by melt infiltration. *Mater Sci Eng A* 2012;549:228–32.
- [11] Altenaiji M, Guan ZW, Cantwell WJ, Zhao Y, G.K. Schleyer. Characterisation of aluminium matrix syntactic foams under drop weight impact. *Mater Des* 2014;59:296–302.
- [12] Altenaiji M, Guan ZW, Cantwell W, Zhao YY. Characterisation of Aluminium Matrix Syntactic Foams Dynamic Loading. *Adv Mech Manuf Eng* 2014;564:449–54.
- [13] Lin YF, Zhang Q, Wu GH. Interfacial microstructure and compressive properties of Al-Mg syntactic foam reinforced with glass cenospheres. *J Alloys Compd*. 2016; 655:301–8.
- [14] Kishore K, Shankar R, Sankaran S. Gradient syntactic foams: tensile strength, modulus and fractographic features. *Mater Sci Eng A*. 2005;412(1-2):153–8.
- [15] Jamil A, Guan ZW, Cantwell WJ. The static and dynamic response of CFRP tube reinforced polyurethane. *Compos Struct* 2017;161:85–92.
- [16] Gupta N, Ricci W. Comparison of compressive properties of layered syntactic foams having gradient in microballoon volume fraction and wall thickness. *Mater Sci Eng A* 2006;427:331–42.
- [17] Movahedi N, Murch GE, Belova IV, Fiedler T. Functionally graded metal syntactic foam: fabrication and mechanical properties. *Mater Des* 2019;168:107652.
- [18] Pham TM, Chen W, Kingston J, Hao H. Impact response and energy absorption of single phase syntactic foam. *Compos Part B* 2018;150:226–33.
- [19] Castro G, Nutt SR, Wenchen X. Compression and low-velocity impact behavior of aluminum syntactic foam. *Mater Sci Eng. A* 2013;578:222–9.
- [20] Broxtermann S, Vesenjak M, Krstulovic-Opara L, Fiedler T. Quasi static and dynamic compression of zinc syntactic foams. *J Alloys Compd* 2018;768:962–9.
- [21] Karagiozova D, Alves M. Propagation of compaction waves in cellular materials with continuously varying density. *Int J Solides Struct* 2015;71:323–37.
- [22] Zheng J, Qin Q, Wang T. Impact plastic crushing and design of density-graded cellular materials. *Mech Mater* 2016;94:66–78.
- [23] Rousseau CE, Plume G, Goni M, Ale B. Behavior of syntactic foam under plate impact. *Mech Res Commun* 2017;83:1–5.
- [24] Rostilov TA, Ziborov VS. Experimental study of shock wave structure in syntactic foams under high- velocity impact. *Acta Astronaut* 2021;178:900–7.
- [25] Zhao YY. Metal matrix syntactic foams: Manufacture, matrix material, microstructure, modulus and more. *JOM* 2011;63(2):35.
- [26] Al-Sahlani K, Kisi E, Fiedler T. Impact of particle strength and matrix ductility on the deformation mechanism of metallic syntactic foam. *J Alloys Compd* 2019;786:292–9.
- [27] Gupta N, Shunmugasamy VC. High strain rate compressive response of syntactic foams: trends in mechanical properties and failure mechanisms. *Mater Sci Eng A*. 2011;528:7596–605.
- [28] Goel MD, Mondal DP, Yadav MS, Gupta SK. Effect of strain rate and relative density on compressive deformation behavior of aluminum cenosphere syntactic foam. *Mater Sci Eng A*. 2014;590:406–15.
- [29] Zhang BY, Lin YF, L S, Zhai DX, Wu GH. Quasi-static and high strain rates compressive behavior of aluminium matrix syntactic foams. *Compos Part B*. 2016; 98:288–96.
- [30] Mondal DP, Jha N, Badkul A, Das S, Khedle R. High temperature compressive deformation behaviour of aluminum syntactic foam. *Mater Sci Eng A* 2012;534:521–9.
- [31] Song B, Chen W, Yanagita T, Frew DJ. Confinement effects on the dynamic compressive properties of an epoxy syntactic foam. *Compos Struct* 2005;67:279–87.
- [32] Johnson W. Impact strength of materials. Edward Arnold London; 1972. p. 225–9.
- [33] Rieder KA, Mindess S. New test method to evaluate the impact behaviour of biaxially confined concrete. *Mater Struct* 1998;31(10):669–75.